

# Hierarchical Amortized Training for Memory-efficient High Resolution 3D GAN

Li Sun, Junxiang Chen, Yanwu Xu, Mingming Gong, Ke Yu, and Kayhan Batmanghelich\*

**Abstract**—Generative Adversarial Networks (GAN) have many potential medical imaging applications, including data augmentation, domain adaptation, and model explanation. Due to the limited embedded memory of Graphical Processing Units (GPUs), most current 3D GAN models are trained on low-resolution medical images. In this work, we propose a novel end-to-end GAN architecture that can generate high-resolution 3D images. We achieve this goal by separating training and inference. During training, we adopt a hierarchical structure that simultaneously generates a low-resolution version of the image and a randomly selected sub-volume of the high-resolution image. The hierarchical design has two advantages: First, the memory demand for training on high-resolution images is amortized among subvolumes. Furthermore, anchoring the high-resolution subvolumes to a single low-resolution image ensures anatomical consistency between subvolumes. During inference, our model can directly generate full high-resolution images. We also incorporate an encoder with a similar hierarchical structure into the model to extract features from the images. Experiments on 3D thorax CT and brain MRI demonstrate that our approach outperforms state of the art in image generation and clinical-relevant feature extraction.

**Index Terms**—Generative Adversarial Networks, 3D Image Synthesis, High Resolution.

## I. INTRODUCTION

GENERATIVE Adversarial Networks (GANs) have succeeded in generating realistic-looking images in Computer Vision [1]–[3]. It has shown potential in medical imaging for augmentation [4], [5], image reconstruction [6] and image-to-image translation [7], [8]. The prevalence of 3D images in the radiology domain renders the real-world application of GANs in the medical domain even more challenging than the natural image domain. In this paper, we propose an efficient method for generating and extracting features from high-resolution volumetric images.

The training procedure of GANs corresponds to a min-max game between two players: a generator and a discriminator. While the generator aims to generate realistic-looking images,

the discriminator aims to defeat the generator by recognizing real from the fake (generated) images. When the field of view (FOV) is the same, a higher resolution is equivalent to more voxels. In this way, we use “high-resolution image” and “large-size image” interchangeably in the paper. Training GANs for high-resolution 3D images is more difficult than 2D images because the memory demand of the model grows cubically with the size of the image [9]. Most of the existing 3D GAN models are trained on low-resolution 3D images (*e.g.*,  $128^3$  or below) to avoid memory overflow [5], [6], [10]. One commonly adopted strategy for high-resolution 3D image generation is through slice-wise [8] or patch-wise [10] generation. However, these methods usually introduce artifacts between patches and slices due to inconsistency between adjacent slices. More related work can be found in Section III.

In this paper, we introduce a Hierarchical Amortized GAN (HA-GAN). Our model has training and inference phases separated. In the training phase, we simultaneously generate a low-resolution image and a randomly selected sub-volume of the high-resolution image. Generating sub-volumes amortizes the memory cost of the high-resolution image and keeps local details of the 3D image. Furthermore, the low-resolution image ensures anatomical consistency and the global structure of the generated images. We train the model in an end-to-end fashion while retaining the memory efficiency. The gradients of the parameters, which are the memory bottleneck, are needed only during training. Hence, subvolume selection is no longer needed and the entire high-resolution volume can be generated during inference. In addition, we implement an encoder in a similar fashion. The encoder enables us to extract features from a given image and prevents the model from mode collapse. We test HA-GAN on thorax CT and brain MRI datasets. Experiments demonstrate that our approach outperforms baselines in image generation and clinical-relevant feature extraction. We also present a clinical application of cross-modality transform with conditional HA-GAN, which can assist clinical treatment [11]. Our code will be made publicly available.

In summary, we make the following contributions:

- 1) We introduce a novel end-to-end HA-GAN architecture that can generate high-resolution volumetric images while being memory efficient.
- 2) We incorporate a memory-efficient encoder with a similar structure, enabling clinical-relevant feature extraction from high-resolution 3D images. We show that the encoder improves generation quality.
- 3) We discover that moving along specific directions in latent space results in explainable anatomical variations

Manuscript received Jan 10, 2021. This work was partially supported by NIH Award Number 1R01HL141813-01, NSF 1839332 Tripod+X, and SAP SE. We are grateful for the computational resources provided by Pittsburgh SuperComputing grant number TG-ASC170024. *Asterisk indicates corresponding author.*

L. Sun, Y. Xu and K. Yu are with the School of Computing and Information, University of Pittsburgh, Pittsburgh, PA 15206, USA (email: lis118@pitt.edu, yanwuxu@pitt.edu, key44@pitt.edu)

J. Chen and K. Batmanghelich are with the Department of Biomedical Informatics, University of Pittsburgh, Pittsburgh, PA 15206, USA (email: juc91@pitt.edu, kayhan@pitt.edu)

M. Gong is with the School of Mathematics and Statistics, The University of Melbourne, Parkville, VIC, Australia (e-mail: mingming.gong@unimelb.edu.au).

in generated images.

- 4) We evaluate our method by extensive experiments on different image modalities as well as different anatomy. The HA-GAN offers significant quantitative and qualitative improvements over the state-of-the-art.

## II. METHOD

We first review Generative Adversarial Networks (GANs) in Section II-A. Then, we introduce our method in Section II-B, followed by the introduction of the encoder in Section II-C. We conclude this section with the optimization scheme in Section II-D and the implementation details in Section II-E. The notations used are summarized in Table I.

TABLE I: Important notations in this paper

Models	
$G^A(\cdot)$	The common block of the generator.
$G^L(\cdot)$	The low-resolution block of the generator.
$G^H(\cdot)$	The high-resolution block of the generator.
$D^H(\cdot)$	The discriminator for high-resolution images.
$D^L(\cdot)$	The discriminator for low-resolution images.
$E^H(\cdot)$	The high-resolution block of the encoder.
$E^G(\cdot)$	The ground block of the encoder.
Functions	
$S^H(\cdot, \cdot)$	The high-resolution sub-volume selector.
$S^L(\cdot, \cdot)$	The low-resolution sub-volume selector.
Variables	
$Z$	Latent representations.
$\hat{Z}$	Reconstructed latent representations.
$r$	The index of the starting slice for sub-volume selection.
$X^H$	The high-resolution real image.
$X^L$	The low-resolution real image.
$\hat{X}^H$	The generated high-resolution image.
$\hat{X}_r^H$	The generated high-resolution sub-volume starting at slice $r$ .
$\hat{X}^L$	The generated low-resolution image.
$A$	Intermediate feature maps for the whole image
$A_r$	Intermediate feature maps for the sub-volume starting at slice $r$
$\hat{A}$	Reconstructed intermediate feature maps for the whole image.
$\hat{A}_v$	Reconstructed intermediate feature maps for the $v$ -th sub-volume.
$\{T_v\}_{v=1}^V$	The indices of the starting slices for a partition for $X^H$ .

### A. Background

Generative Adversarial Networks (GANs) [1] is widely used to generate realistic-looking images. The training procedure of GANs corresponds to a two-player game that involves a generator  $G$  and a discriminator  $D$ . In the game, while  $G$  aims to generate realistic-looking images,  $D$  tries to discriminate real images from the images synthesized by  $G$ . The  $D$  and  $G$  compete with each other. Let  $P_X$  denote the underlying data distribution, and  $P_Z$  denote the distribution of the random noise  $Z$ . Then the objective of GAN is formulated as below:

$$\min_G \max_D \mathbb{E}_{X \sim P_X} [\log D(X)] + \mathbb{E}_{Z \sim P_Z} [\log(1 - D(G(Z)))]. \quad (1)$$

### B. The Hierarchical Structure

**Generator** Our generator has two branches that generate the low-resolution image  $\hat{X}^L$  and a randomly selected sub-volume of the high-resolution image  $\hat{X}_r^H$ , where  $r$  represents

the index for the starting slice of the sub-volume. The two branches share initial layers  $G^A$  and after they branch off:

$$\hat{X}^L = G^L(\underbrace{G^A(Z)}_A), \quad (2)$$

$$\hat{X}_r^H = G^H(\underbrace{S^L(G^A(Z); r)}_{A_r}), \quad (3)$$

where  $G^A(\cdot)$ ,  $G^L(\cdot)$  and  $G^H(\cdot)$  denote the common, low-resolution and high-resolution blocks of the generator, respectively.  $S^L(\cdot, r)$  is a selector function that returns the sub-volume of input image starting at slice  $r$ , where the superscript  $L$  indicates that the selection is done at low resolution. The output of this function is fed into  $G^H(\cdot)$ , which lift the input to the high resolution. We use  $A$  and  $A_r$  as short-hand notation for  $G^A(Z)$  and  $S^L(G^A(Z); r)$ , respectively. We let  $Z \sim \mathcal{N}(\mathbf{0}, \mathbf{I})$  be the input random noise vector. We let  $r$  be the randomly selected index for the starting slice that is drawn from a uniform distribution, denoted as  $r \sim \mathcal{U}$ ; i.e., each slice is selected with the same probability. The schematic of the proposed method is shown in Fig. 1. Note that  $\hat{X}_r^H$  depends on a corresponding sub-volume of  $A$ , which is  $A_r$ . Therefore, we feed  $A_r$  rather than complete  $A$  into  $G^H$  during training, making the model memory-efficient.

**Discriminator** Similarly, we define two discriminators  $D^H$  and  $D^L$  to distinguish a real high-resolution sub-volume  $X_r^H$  and a low-resolution image  $X^L$  from the fake ones, respectively.  $D^H$  makes sure that the local details in the high-resolution sub-volume look realistic. At the same time,  $D^L$  ensures the proper global structure is preserved. Since we feed a sub-volumes  $S^H(X^H; r)$  rather than the entire image  $X^H$  into  $D^H$ , the memory cost of the model is reduced.

There are two GAN losses  $\mathcal{L}_{GAN}^H$  and  $\mathcal{L}_{GAN}^L$  for low and high resolutions respectively:

$$\begin{aligned} \mathcal{L}_{GAN}^H(G^A, G^H, D^H) = & \min_{G^H, G^A} \max_{D^H} \mathbb{E}_{r \sim \mathcal{U}} \left[ \mathbb{E}_{X \sim P_X} [\log D^H(S^H(X^H; r))] \right. \\ & \left. + \mathbb{E}_{Z \sim P_Z} [\log(1 - D^H(\hat{X}_r^H))] \right], \end{aligned} \quad (4)$$

$$\begin{aligned} \mathcal{L}_{GAN}^L(G^L, G^A, D^L) = & \min_{G^L, G^A} \max_{D^L} \mathbb{E}_{X \sim P_X} [\log D^L(X^L)] \\ & + \mathbb{E}_{Z \sim P_Z} [\log(1 - D^L(\hat{X}^L))]. \end{aligned} \quad (5)$$

Note that the sampler  $S^H(\cdot; r)$  in Equation (3) and  $S^L(\cdot; r)$  in Equation (4) are synchronized, such that  $r$  correspond to the indices for the same percentile of slices in the high- and low-resolution.

**Inference** The memory space needed to store gradient is the main bottleneck for 3D GANs models; however, the gradient is not needed during inference. Therefore, we can directly generate the high-resolution image by feeding  $Z$  into  $G^A$  and  $G^H$  sequentially, i.e.,  $\hat{X}^H(Z) = G^H(G^A(Z))$ . Note that to generate the entire image during inference, we directly feed the complete feature maps  $A = G^A(Z)$  rather than its sub-volume  $A_r$  into the convolutional network  $G^H$ . The idea is illustrated at the top of Fig. 2.

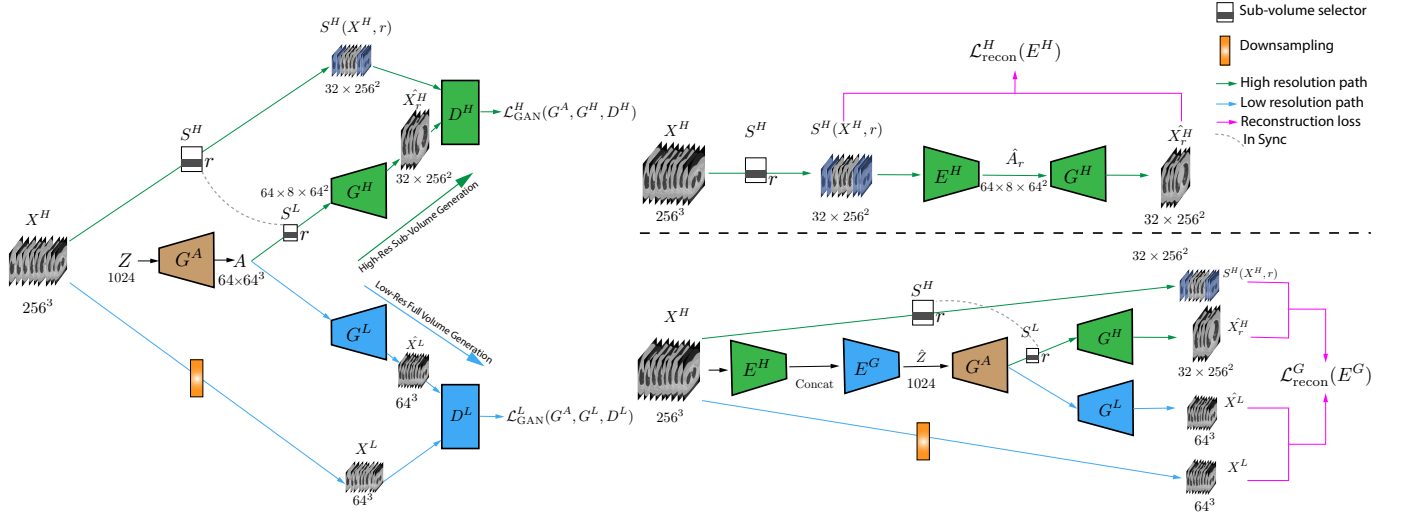


Fig. 1: **Left:** The schematic of the model (without encoder). At the training time, instead of directly generating high-resolution full volume, our generator contains two branches for high-resolution sub-volume and low-resolution full volume generation, respectively. The two branches share the common block  $G^A$ . A sub-volume selector is used to select a part of the intermediate feature for the sub-volume generation. **Right:** The Schematic of the hierarchical encoder trained with two reconstruction losses, one on the high-resolution sub-volume level (upper right) and another one on the low-res full volume level (lower right). The meanings of the notations used can be found in Table I. The model adopts 3D architecture with details presented in **Supplementary Material**.

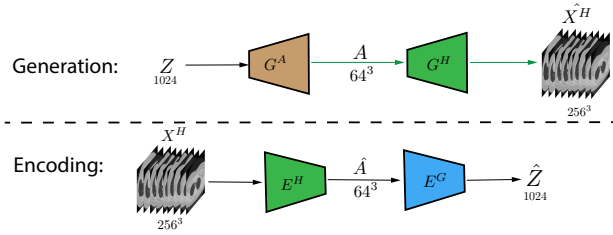


Fig. 2: Inference with the hierarchical generator and encoder. Since there is no need for gradient storage at inference time, the memory demand is lower and sub-volume selection is no longer needed. We directly forward input through the high-res branch for high-res full image generation and encoding.

### C. Incorporating the Encoder

We also adopt a hierarchical structure for the encoder, by defining two encoders  $E^H(\cdot)$  and  $E^G(\cdot)$  encoding the high-resolution sub-volume and the entire image respectively. We partition the high-resolution image  $X^H$  into a set of  $V$  *non-overlapping* sub-volumes, i.e.,  $X^H = \text{concat}(\{S^H(X^H, T_v)\}_{v=1}^V)$ , where  $\text{concat}$  represent concatenation,  $S^H(\cdot)$  represents the selector function that returns a sub-volume of a high-resolution image, and  $T_v$  represents the corresponding starting indices for the non-overlapping partition.

We use  $\hat{A}_v$  to denote the sub-volume-level feature maps for the  $v$ -th sub-volume, i.e.,  $\hat{A}_v = E^H(S^H(X^H; T_v))$ . To generate the image-level representation  $\hat{Z}$ , we first summarize all sub-volume representation for the image through concatenation, such that  $\hat{A} = \text{concat}(\{\hat{A}_v\}_{v=1}^V)$ . Then we feed  $\hat{A}$  into the encoder  $E^G(\cdot)$  to generate the image-level representation  $\hat{Z}$ , i.e.,  $\hat{Z} = E^G(\hat{A})$ .

In order to obtain optimal  $E^H$  and  $E^G$ , we introduce the following objective functions:

$$\mathcal{L}_{recon}^H(E^H) = \min_{E^H} \mathbb{E}_{X \sim P_X, r \in U} \|S^H(X^H; r) - G^H(\hat{A}_r)\|_1, \quad (6)$$

$$\mathcal{L}_{recon}^G(E^G) = \min_{E^G} \mathbb{E}_{X \sim P_X} [\|X^L - G^L(G^A(\hat{Z}))\|_1 + \mathbb{E}_{r \sim U} [\|S^H(X^H; r) - G^H(S^L(G^A(\hat{Z}); r))\|_1]]. \quad (7)$$

Equation (6) ensures a randomly selected high-resolution sub-volume  $S^H(X^H; r)$  can be reconstructed. Equation (7) enforces both the low-resolution image  $X^L$  and a random selected  $S^H(X^H; r)$  can be reconstructed given  $\hat{Z}$ . Note that in Equation (6), the sub-volume is reconstructed from the intermediate feature maps  $\hat{A}_v$ ; while in the second term in Equation (7), the sub-volume is reconstructed from the latent representations  $\hat{Z}$ . In these equations, we use  $\ell_1$  loss for reconstruction because it tends to generate sharper result compared to  $\ell_2$  loss [12]. The structure of the encoders are illustrated in Fig. 1.

When optimizing for Equation (6), we only update  $E^H$  while keeping all other parameters fixed. Similarly, when optimizing for Equation (7), we only update  $E^G$ . We empirically find that this optimization strategy is memory-efficient and leads to better performance.

**Inference** In the inference phase, we can get the latent code  $\hat{Z}$  by feeding the sub-volumes of  $X^H$  into  $E^H$ , concatenating the output sub-volume feature maps into  $\hat{A}$  and then feeding the results into  $E^G$ , i.e.,  $\hat{Z} = E^G(\text{concat}(\{E^H(S^H(X^H; T_v))\}_{v=1}^V))$ . The idea is illustrated at the bottom of Fig. 2.

#### D. Overall Model

The model is trained in an end-to-end fashion. The overall loss function is defined as:

$$\mathcal{L} = \mathcal{L}_{GAN}^H(G^H, G^A, D^H) + \mathcal{L}_{GAN}^L(G^L, G^A, D^L) + \lambda_1 \mathcal{L}_{recon}^H(E^H) + \lambda_2 \mathcal{L}_{recon}^G(E^G), \quad (8)$$

where  $\lambda_1$  and  $\lambda_2$  control the trade-off between the GANs losses and the reconstruction losses. The optimizations for generator ( $G^H$ ,  $G^L$  and  $G^A$ ), discriminator ( $D^H$ ,  $D^L$ ), and encoder ( $E^H$ ,  $E^G$ ) are altered per iteration.

#### E. Implementation Details

We train the proposed HA-GAN for ten epochs, the training and validation curves can be found in Supplementary Material. We let the learning rate for generator, encoder, and discriminator to be  $1 \times 10^{-4}$ ,  $1 \times 10^{-4}$ , and  $4 \times 10^{-4}$ , respectively. We also employed  $\beta_1 = 0$  and  $\beta_2 = 0.999$  in the Adam optimizer. The batch size is set as 4. We let the size of the  $X^L$  be  $64^3$ . The size of the randomly selected sub-volume  $S^H(X^H; r)$  is defined to be  $32 \times 256^2$ , where  $r$  is randomly selected on the batch level. We let feature maps  $A$  have 64 channels with a size of  $64^3$ . The dimension of the latent variable  $Z$  is chosen to be 1,024. The trade-off hyper-parameters  $\lambda_1$  and  $\lambda_2$  are set to be 5. The experiments are performed on two NVIDIA Titan Xp GPUs, each with 12GB GPU memory. The detailed architecture can be found in **Supplementary Material**.

### III. RELATED WORK

In the following, we review the works related to GANs for medical images, memory-efficient 3D GAN and representation learning in generative models.

#### A. GANs for Medical Images

In recent years, researchers have developed GAN-based models for medical images. These models are applied to solve various problems, including image synthesis [13]–[15], data augmentation [5], [16], image reconstruction, [17], [18], modality/style transformation [19], [20], segmentation [21], [22], and model explanation [23]. However, most of these methods concentrate on generating 2D medical images. In this paper, we focus on solving a more challenging problem, i.e., generating 3D images.

With the prevalence of 3D imaging in medical applications, 3D GAN models become a popular research topic. Shan et al. [24] proposed a 3D conditional GAN model for low-dose CT denoising. Kudo et al. [25] proposed a 3D GAN model for CT image super-resolution. Jin et al. [26] propose an auto-encoding GAN for generating 3D brain MRI images. Cirillo et al. [27] proposed to use a 3D model conditioned on multi-channel 3D Brain MR images to generate tumor mask for segmentation. While these methods can generate realistic-looking 3D MRI or CT images, the generated images are limited to the small size of  $128 \times 128 \times 128$  or below, due to insufficient memory during training. In contrast, our HA-GAN is a memory-efficient model and can generate 3D images with a size of  $256 \times 256 \times 256$ .

#### B. Memory-Efficient GANs

Some works are proposed to reduce the memory demand of high-resolution 3D image generation. In order to address the memory challenge, some works adopt slice-wise [8] or patch-wise [10] generation approach. Unfortunately, these methods may introduce artifacts at the intersection between patches/slices because they are generated independently. To remedy this problem, Uzunova et al. [9] propose a multi-scale approach that uses a GAN model to generate a low-resolution version of the image first. An additional GAN model is used to generate higher resolution patches of images conditioned on the previously generated patches of lower resolution images. However, this method is still patch-based; the generation of local patches is unaware of the global structure, potentially leading to spatial inconsistency. In addition, the model is not trained in an end-to-end manner, which makes it challenging to incorporate an encoder that learns the latent representations for the entire images. In comparison, our proposed HA-GAN is global structure-aware and can be trained end-to-end. This allows HA-GAN to be associated with an encoder.

#### C. Representation Learning in Generative Models

Several existing generative models are fused with an encoder [3], [28], [29], which learns meaningful representations for images. These methods are based on the belief that a good generative model that reconstructs realistic data will automatically learn a meaningful representation of it [30]. A generative model with an encoder can be regarded as a compression algorithm [31]. Hence, the model is less likely to suffer from mode collapse because the decoder is required to reconstruct all samples in the dataset, which is impossible if mode collapse happens such that only limited varieties of samples are generated [3]. Variational autoencoder (VAE) [28] uses an encoder to compress data into a latent space, and a decoder is used to reconstruct the data using the encoded representation. BiGAN [29] learns a bidirectional mapping between data space and latent space.  $\alpha$ -GAN [3] introduces not only an encoder to the GAN model, but also learns a disentangled representation by implementing a code discriminator, which forces the distribution of the code to be indistinguishable from that of random noise. Variational auto-encoder GAN (VAE-GAN) [32] adds an adversarial loss to the variational evidence lower bound objective. Despite their success, the methods mentioned above can analyze 2D images or low-resolution 3D images, which are less memory intensive for training an encoder. In contrast, our proposed HA-GAN is memory efficient and can be used to encode and generate high-resolution 3D images during inference.

### IV. EXPERIMENTS

We evaluate the proposed model's performance in two aspects: image synthesis and clinical-relevant feature extraction. We also explore the semantic meaning of the latent variable. We perform 5-fold cross-validation for the experiments. We compare our method with baseline methods, including WGAN [33], VAE-GAN [32],  $\alpha$ -GAN [6] and Progressive GAN [34]. We set the size of the latent variable to be 1000, following the practice in [6].

### A. Datasets

The experiments are conducted on two large-scale medical datasets, including the COPDGene dataset [35] and the GSP dataset [36]. Both datasets are publicly available and details about image acquisition can be found in Supplementary Material.

**COPDGene Dataset:** We use 3D thorax computerized tomography (CT) images of 9,276 subjects from COPDGene dataset in our study. We trim blank slices with all-zero values and resize the images to  $256^3$ . The Hounsfield Units (HU) are mapped to the intensity window of  $[-1024, 600]$  and normalized to  $[-1, 1]$ .

**GSP Dataset:** We use 3D Brain magnetic resonance images (MRIs) of 3,538 subjects from Brain Genomics Superstruct Project (GSP) [36] in our experiments. The FreeSurfer package [37] is used to remove the non-brain region in the images, bias-field correction, intensity normalization, affine registration to Talairach space, and resampling to  $1mm^3$  isotropic resolution. We trim the blank slices with all-zero values and rescale the images into  $256^3$ . The intensity value is normalized to  $[-1, 1]$ .

### B. Image Synthesis

We examine whether the synthetic images are realistic-looking quantitatively and qualitatively, where synthetic images are generated by feeding random noise into the generator.

1) *Quantitative Evaluation:* If the synthetic images are realistic-looking, then the synthetic images' distribution should be indistinguishable from that of the real images. Therefore, we can quantitatively evaluate the quality of the synthetic images by computing Fréchet Inception Distance (FID) [38] and Maximum Mean Discrepancy (MMD) [39] between the distributions of real images and synthetic images. Lower values of these quantities indicate that the distributions are more similar, implying more realistic-looking synthetic images. We evaluate the synthesis quality at two resolutions:  $128^3$  and  $256^3$ . Due to memory limitations, the baseline models can only be trained with the size of  $128^3$  at most. To make a fair comparison with our model (HA-GAN), we apply nearest-neighbor interpolation to upsample the synthetic images of baseline models to  $256^3$ . We adopt a 3D ResNet model pre-trained on 3D medical images [40] to extract features for computing FID. Note the scale of FID relies on the feature extraction model. Thus our FID values are not comparable to FID value calculated on 2D images, which is based on feature extracted using model pre-trained on ImageNet. As shown in Table II, HA-GAN achieves lower FID and MMD compared to the baselines, which implies that HA-GAN generates more realistic images. We found that at the resolution of  $128^3$ , HA-GAN still outperforms the baseline models, but the lead has been smaller compared with result at the resolution of  $256^3$ . In addition, we performed statistical tests on the evaluation results at  $256^3$  resolution between methods. More specifically, we performed two-sample  $t$ -tests (one-tailed) between HA-GAN and each of the baseline method. The results are shown in Table III. At a significance level of 0.05, HA-GAN achieves

significantly higher performance than baseline methods for both datasets.

2) *Ablation Study:* We perform three ablation studies to validate the contribution of each of the proposed components. The experiments are performed at  $256^3$  resolution. Shown in Table IV, we found that adding a low-resolution branch can help improve results, since it can help the model learn the global structure. Adding an encoder can also help improve performance, since it can help stabilize the training. For the deterministic  $r$  experiments, we make the sub-volume selector to use a set of deterministic values of  $r$  (equal interval between them) rather than the randomly sampled  $r$  currently used. From the results, we can see that randomly sampled  $r$  outperforms deterministic  $r$ .

3) *Qualitative Evaluation:* To qualitatively analyze the results, we show some samples of synthetic images in Fig. 3. The figure illustrates that HA-GAN generates sharper images than the baselines. More high-resolution samples and latent space interpolation are provided in **Supplementary Material**.

To illustrate whether the synthetic images look similar to the real ones, we embed the synthetic and real images into the same space. If the synthetic images are indistinguishable from the real images, then we expect that the synthetic and real images occupy the same region in the embedding space. Following the practice of [6], we first use a pretrained 3D medical ResNet model [40] to extract features for 512 synthetic images by each method. As a reference, we also extract features for the real image samples using the same ResNet model. Then we conduct MDS to embed the extracted features into 2-dimensional space for both COPDGene and GSP datasets. The results are visualized in Fig. 5a and 5b, respectively. In both figures, we fit an ellipse for the embedding of each model with the least square. In the figures, we observe that synthetic images by HA-GAN better overlap with real images, compared with the baselines. This implies that HA-GAN generates more realistic-looking images than the baselines. We also provide PCA and tSNE visualization results in Supplementary Material.

### C. Clinical-Relevant Feature Extraction

We evaluate the encoded latent variables from real images in ways: First, we test how well the encoded variables can be used to recover the original image. If the original image can be recovered well, then the latent variable contains most of information about the original images. This task can be challenging because the size of the encoded variable is extremely smaller than original images, thus losing details is nearly inevitable. Second, we use the encoded variable to predict clinical-relevant measurements. This task is used to evaluate how much information about the disease severity is preserved in the encoded latent features.

1) *Image Recovery:* In this task, we first encode held-out images from the test set using the trained encoder. Then the original images are recovered by forwarding the encoded latent variable to the trained generator. We use three metrics to evaluate the quality of image recovery: SSIM (Structural Similarity Index, higher is better) [41], NMSE (Normalized

TABLE II: Evaluation for image synthesis

Dataset	COPDGene (Lung)				GSP (Brain)			
Resolution	128 <sup>3</sup>		256 <sup>3</sup>		128 <sup>3</sup>		256 <sup>3</sup>	
	FID↓	MMD↓	FID↓	MMD↓	FID↓	MMD↓	FID↓	MMD↓
WGAN	0.012±.011	0.092±.059	0.058±.025	0.335±.064	0.006±.002	0.406±.143	0.011±.005	0.227±.044
VAE-GAN	0.139±.002	1.065±.008	0.331±.008	1.030±.009	0.075±.004	0.667±.026	0.617±.046	0.701±.028
α-GAN	0.010±.004	0.089±.056	0.043±.016	0.145±.054	0.010±.007	0.606±.204	0.012±.007	0.222±.096
Progressive GAN	0.015±.007	0.150±.072	0.070±.016	0.182±.047	0.017±.008	0.818±.217	0.066±.032	0.753±.247
HA-GAN	<b>0.005±.003</b>	<b>0.038±.020</b>	<b>0.008±.003</b>	<b>0.022±.010</b>	<b>0.002±.001</b>	<b>0.129±.026</b>	<b>0.004±.001</b>	<b>0.086±.029</b>

TABLE III: Statistical test for comparison of image synthesis. Null hypothesis: The mean of distance metric (FID and MMD) of HA-GAN is equal or higher than baseline method.

Dataset	COPDGene (Lung)		GSP (Brain)	
p-value	FID	MMD	FID	MMD
WGAN	$2 \times 10^{-3}$	$< 1 \times 10^{-3}$	0.01	$< 1 \times 10^{-3}$
VAE-GAN	$< 1 \times 10^{-6}$	$< 1 \times 10^{-6}$	$< 1 \times 10^{-6}$	$< 1 \times 10^{-6}$
α-GAN	$2 \times 10^{-3}$	$1 \times 10^{-3}$	0.02	$9 \times 10^{-3}$
Progressive GAN	$< 1 \times 10^{-3}$	$< 1 \times 10^{-3}$	$3 \times 10^{-3}$	$< 1 \times 10^{-3}$

Mean Square Error, lower is better), and PSNR (Peak Signal-to-Noise Ratio, higher is better). Table V shows that HA-GAN outperforms baselines in terms of image recovery. In addition, we performed paired two-sample  $t$ -tests (one-tailed) between HA-GAN and each baseline method on the evaluation metrics (SSIM, NMSE and PSNR). The null hypothesis is that the mean of distance metric (SSIM, NMSE and PSNR) of HA-GAN is equal or worse than baseline method. The results are shown in Table VI. At a significance level of 0.05, the null hypothesis is rejected and HA-GAN achieves significantly higher performance than baseline methods for both datasets. A few examples of the recovered images are shown in Fig. 3. Note that we do not include the results of WGAN and Progressive GAN, because they do not incorporate an encoder.

We expect that if images are well recovered, each brain structure in the recovered image is consistent with the original images. Hence, to evaluate the image encoding quality on structure level, we use FreeSurfer [37] to segment a representative subset of 12 brain ROIs from real brain images and recovered brain images, including cerebral white matter (WM) and cortex (CT), lateral ventricle (LV), cerebellar white matter (CW) and cortex (CC), thalamus (TH), caudate (CA); putamen (PU), pallidum (PA), brainstem (BS), hippocampus (HP), and amygdala (AM). Dice score is used to evaluate the performance. Fig. 6 shows that the proposed HA-GAN outperforms baseline models in almost all structures with highest Dice scores.

2) *Predicting clinical-relevant measurements*: This section discusses how much information about the disease severity is preserved in the encoded latent features. We select two respiratory measurements and one CT-based measurements of emphysema to measure disease severity. For respiratory measurements, we use percent predicted values of Forced Expiratory Volume in one second (FEV1<sub>pp</sub>) and its ratio with Forced vital capacity (FVC) (FEV1/FVC). Given extracted features, we train a Ridge regression model with  $\lambda = 1 \times 10^{-4}$  to predict the *logarithm* of each of the measurements. We report the  $R^2$  scores on held-out test data. The Table VII

shows that HA-GAN achieves higher  $R^2$  than the baselines. The results imply that HA-GAN preserves more information about the disease severity than baselines.

#### D. Exploring the Latent Space

This section investigates whether change along a certain direction in the latent space corresponds to semantic meanings. We segment the lung regions in the thorax CT images using Chest Image Platform (CIP) [42], and segment the fat tissues [43], bone tissues and emphysema regions [44] via thresholding, the detailed thresholding criteria can be found in Supplementary Material. We segment the brain, hippocampus, and lateral ventricle for the synthetic brain MRIs with the FreeSurfer package [37]. Next, we train linear regression models that predict the total volume of the different tissues/regions with the encoded latent representations  $Z$  for each image, optimizing with least square. The learnt parameter vector for each class represents the latent direction. Then, we manipulate the latent variable along the direction corresponding to the learned parameters of linear models and generate the images by feeding the resulted latent representations into the generator. More specifically, first a reference latent variable is randomly sampled, then the latent variable is moved along the latent direction learnt until the target volume is reached, which is predicted by the linear regression model. As shown in Fig. 7, for thorax CT images, we identify directions in latent space corresponding to the volume of lung, fat, bone and emphysema, respectively. As shown in Fig. 7, for brain MRIs, we identify directions in latent space corresponding to the volume of brain, hippocampus, and lateral ventricles, respectively. When we go along these directions in latent space, we can observe the change of volumes for these tissues.

#### E. Memory Efficiency

In this section, we compare the memory efficiency of HA-GAN with baselines. We measure the GPU memory usage at the training time for all models under different resolutions, including  $32^3$ ,  $64^3$ ,  $128^3$ , and  $256^3$ . The results are shown in Fig. 9. Note that the experiments are performed on the same GPU (Tesla V100 with 16GB memory), and we set the batch size to 2. The HA-GAN consumes much less memory than baseline models under different resolutions. In addition, HA-GAN is the only model that can generate images of sizes  $256^3$ . All other models exhaust the entire memory of GPU; thus, the memory demand cannot be measured. In order to investigate where the memory efficiency come from, we report the number of parameters for HA-GAN at different resolutions

TABLE IV: Results of ablation study

Dataset	COPDGene (Lung)		GSP (Brain)	
	FID↓	MMD↓	FID↓	MMD↓
HA-GAN w/o low-res branch	0.030±.018	0.071±.039	0.118±.078	0.876±.182
HA-GAN w/o Encoder	0.010±.003	0.034±.006	0.006±.003	0.099±.028
HA-GAN w/ deterministic $r$	0.014±.003	0.035±.007	0.061±.016	0.612±.157
HA-GAN	<b>0.008±.003</b>	<b>0.022±.010</b>	<b>0.004±.001</b>	<b>0.086±.029</b>

TABLE V: Evaluation for image recovery

Dataset	COPDGene (Lung)			GSP (Brain)		
	SSIM ↑	NMSE ↓	PSNR ↑	SSIM ↑	NMSE ↓	PSNR ↑
VAE-GAN	0.398±.038	0.166±.052	15.8±.8	0.751±.025	0.095±.026	22.1±.1
$\alpha$ -GAN	0.293±.042	0.376±.099	11.5±.2	0.753±.020	0.161±.049	19.8±.1
HA-GAN	<b>0.434±.051</b>	<b>0.132±.040</b>	<b>16.4±.8</b>	<b>0.789±.018</b>	<b>0.093±.017</b>	<b>22.2±.8</b>

We do not include the results of WGAN and Progressive GAN, because they do not incorporate an encoder.

TABLE VI: Statistical test for comparison of image recovery. Null hypothesis: The mean of metric (SSIM, NMSE and PSNR) of HA-GAN is equal or worse than baseline method.

Dataset	COPDGene (Lung)			GSP (Brain)		
	SSIM	NMSE	PSNR	SSIM	NMSE	PSNR
VAE-GAN	$< 1 \times 10^{-6}$	$< 1 \times 10^{-6}$	$< 1 \times 10^{-6}$	$< 1 \times 10^{-6}$	$< 1 \times 10^{-6}$	$< 1 \times 10^{-6}$
$\alpha$ -GAN	$< 1 \times 10^{-6}$	$< 1 \times 10^{-6}$	$< 1 \times 10^{-6}$	$< 1 \times 10^{-6}$	$< 1 \times 10^{-6}$	$< 1 \times 10^{-6}$

TABLE VII:  $R^2$  for predicting clinical-relevant measurements

Method	log FEV1pp	log FEV1/FVC	log %Emphysema
VAE-GAN	0.215	0.315	0.375
$\alpha$ -GAN	0.512	0.622	0.738
HA-GAN	<b>0.555</b>	<b>0.657</b>	<b>0.746</b>

We do not include the results of WGAN and Progressive GAN, because they do not incorporate an encoder.

in Table VIII. We found that as the resolution increases, the number of parameters only increases marginally, which is expected as the model would only require a few more layers as resolution increases. We also performed experiments testing the impact of the multiplier factor of the sub-volume selector. More specifically, we measured GPU memory usage under different sizes of sub-volume (e.g. 1/8 of the full volume, 1/4 of the full volume, etc) by controlling the multiplier factor of the sub-volume selector. The results are shown in Table IX. We found that as the multiplier factor increases, the memory usage increases drastically.

In addition, we empirically find that HA-GAN is more computationally efficient compared to baseline models at the 128<sup>3</sup> resolution, see Supplementary Material for more details.

TABLE VIII: Evaluation of model parameters

Output Resolution	Memory Usage (MB)	#Parameters
32 <sup>3</sup>	2573	74.7M
64 <sup>3</sup>	2665	78.7M
128 <sup>3</sup>	3167	79.6M
256 <sup>3</sup>	5961	79.7M

TABLE IX: Evaluation of impact of sub-volume multiplier

Multiplier Factor	Memory Usage (MB)
1/8	5961
1/4	10689
1/2	13185

### F. Cross-modality Transform

In this section, we demonstrate the practical value of HA-GAN using a clinical application: cross-modality transform, which can assist clinical treatment [11]. For this task, we propose a conditional variant of HA-GAN to perform T1-FLAIR cross-modality transform on Multimodal Brain Tumor Image Segmentation Benchmark (BRATS) dataset, which is a Brain MRI dataset. We compare our method with 2D conditional GAN, patch-based 3D conditional GAN and a recently proposed patch-based 3D conditional GAN with local adaptive fusion [10]. The results show that our method outperforms these baseline methods. More experiments details can be found in Supplementary Material.

## V. DISCUSSION

### A. Image Synthesis

As shown quantitatively in Table II, HA-GAN achieves lower FID and MMD, implying that our model generates more realistic images. This is further confirmed by the synthetic images shown in Fig. 3, 4, where HA-GAN generates sharper images compared to other methods. We found that our method outperforms baseline methods at both the resolution of 128<sup>3</sup> and 256<sup>3</sup>, but the lead is larger at 256<sup>3</sup> resolution than 128<sup>3</sup>. Based on the results, we believe that the sharp generation results come from both the model itself and its ability to directly



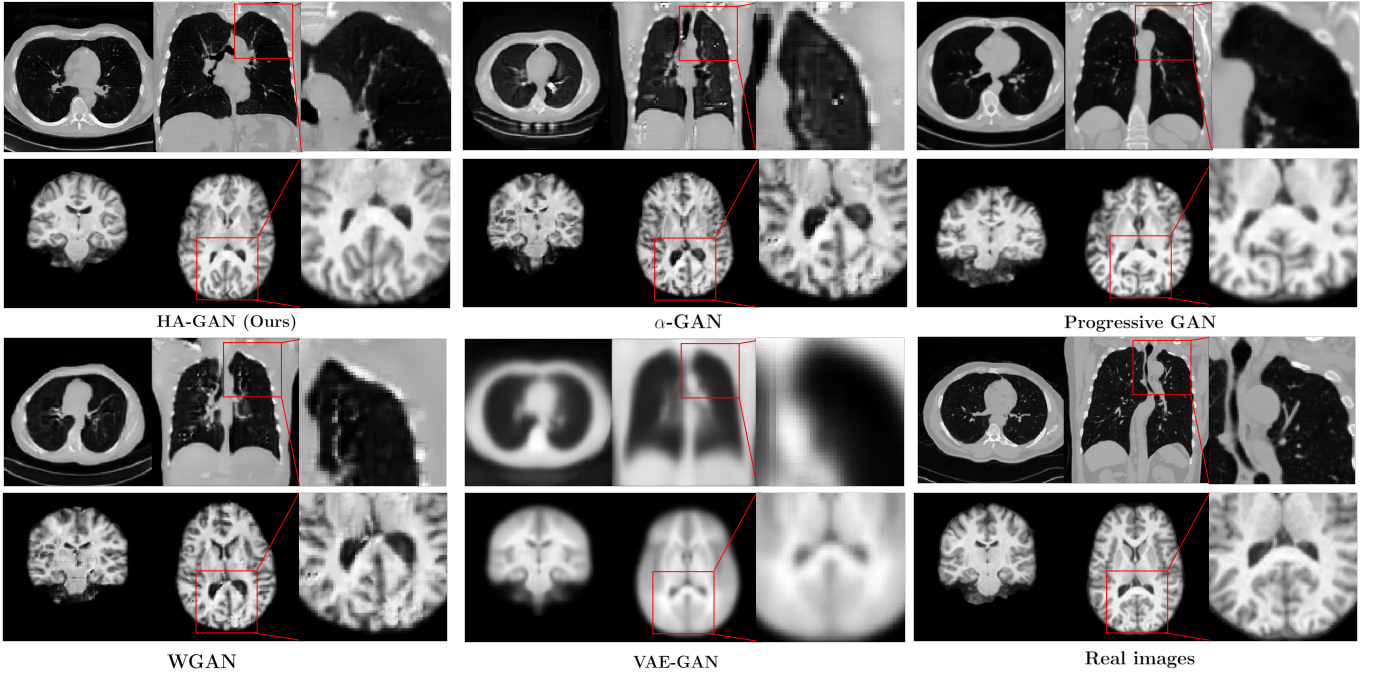


Fig. 3: Randomly generated images from noise by different models and the real images. The figure illustrates that HA-GAN generates sharper images than the baselines.

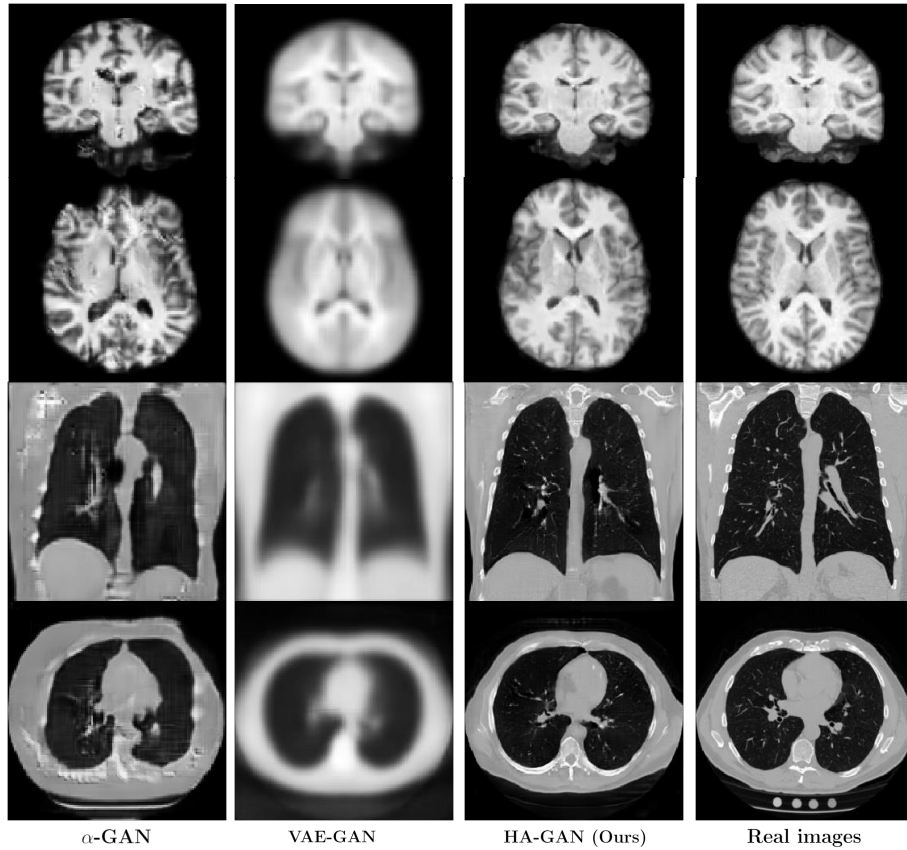


Fig. 4: Recovered images from latent variable by different models. The figure illustrates that features extracted by HA-GAN preserve more information about the original images than the baselines.

generate images at  $256^3$  without interpolation upsampling. For the baseline models, we found that  $\alpha$ -GAN and WGAN have similar performance, and VAE-GAN tends to generate

blurry images. WGAN is essentially the  $\alpha$ -GAN without the encoder. Based on qualitative examples shown in Fig. 3 and supplementary material, it can generate sharper images



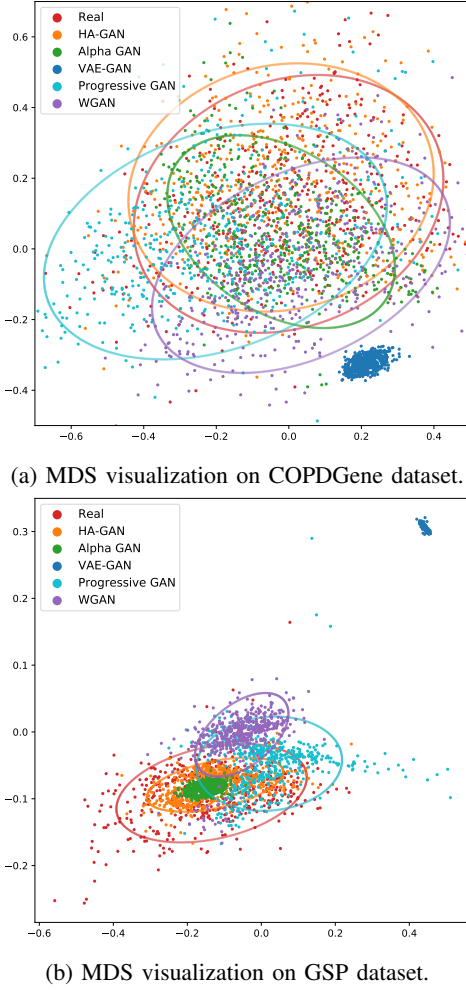


Fig. 5: Comparison of the embedding of different models. We embed the features extracted from synthesized images into 2-dimensional space with MDS. The ellipses are fitted to scatters of each model for better visualization. The figures show that the embedding region of HA-GAN has the most overlapping with real images, compared to the baselines.

compared to  $\alpha$ -GAN and Progressive GAN. However, it also generates more artifacts. According to the quantitative analysis of comparing 1,024 generated images from each model, as shown in Table 2, overall the generation quality of  $\alpha$ -GAN is comparable with WGAN. Although Progressive GAN and  $\alpha$ -GAN also generate realistic-looking images, it can't directly generate images with size  $256^3$  because they are less memory-efficient. Therefore, we have to first generate  $128^3$  images and then interpolate these images into  $256^3$  for a fair comparison. The interpolated images are usually blurry and lack of high-resolution details. In contrast, HA-GAN is memory-efficient and can directly generate images with  $256^3$  size. Therefore, it can generate sharper images with more details.

For the ablation studies, first we found that adding a low-resolution branch can help improve results, we think it's because the low-resolution branch can help the model learn the global structure. Second, we observe in Table IV that HA-GAN with encoder outperforms the version without encoder

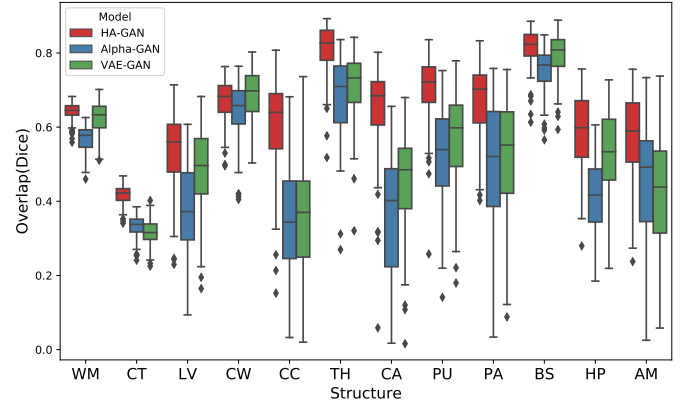


Fig. 6: Dice score on structure-wise recovery (Higher is better). The figures quantitatively measure how much the brain structures in the recovered images overlap with that in the original images. The figures show that HA-GAN achieves higher Dice scores for nearly all of the brain structures, indicating that HA-GAN is capable to more consistently reconstruct each brain structure than the baselines.

in terms of image synthesis quality. This is consistent with the observation in [3] that introducing encoder to GAN improves the quality of synthetic images. When an encoder is introduced to GAN, the reconstruction loss in the objective function ensures that the reconstructed images are voxel-wise consistent with the original images. This term can encourage the generator to represent all data and not to collapse, improving the performance of the generator in terms of image synthesis. Finally, we also see that randomly sampled  $r$  outperforms deterministic  $r$ . We think that this is because using deterministic  $r$  leads to deterministic sub-volume locations, then the generation of junction region between sub-volumes is not learnt well. In comparison, using randomly selected  $r$  leads to randomly selected locations of sub-volumes. In this way, the junctions between sub-volumes can be better covered.

The embedding shown in Fig. 5a and Fig. 5b reveal that the distribution of the synthetic images by HA-GAN is more consistent with the real images, compared to all baselines. The scatters of VAE-GAN seem to be clustered, which indicates that there exists a mode collapse in VAE-GAN. The scatters of WGAN/ $\alpha$ -GAN shows compressed support of real data distribution, which suggests that samples of WGAN/ $\alpha$ -GAN have lower diversity than the real images. However, we observe in 5b that on the GSP dataset, the variance of synthetic images by HA-GAN is smaller than the real images, implying that the generated images are of lower diversity than the real data. We want to improve synthetic diversity by introducing a mini-batch discrimination scheme [45] or using multiple discriminators [46] in future work.

### B. Clinical-Relevant Feature Extraction

We encode the full image into a 1D variable to extract meaningful and compact feature representation for downstream clinical feature prediction. We use the recovery of original image from encoded 1D variable as a way of evaluation of

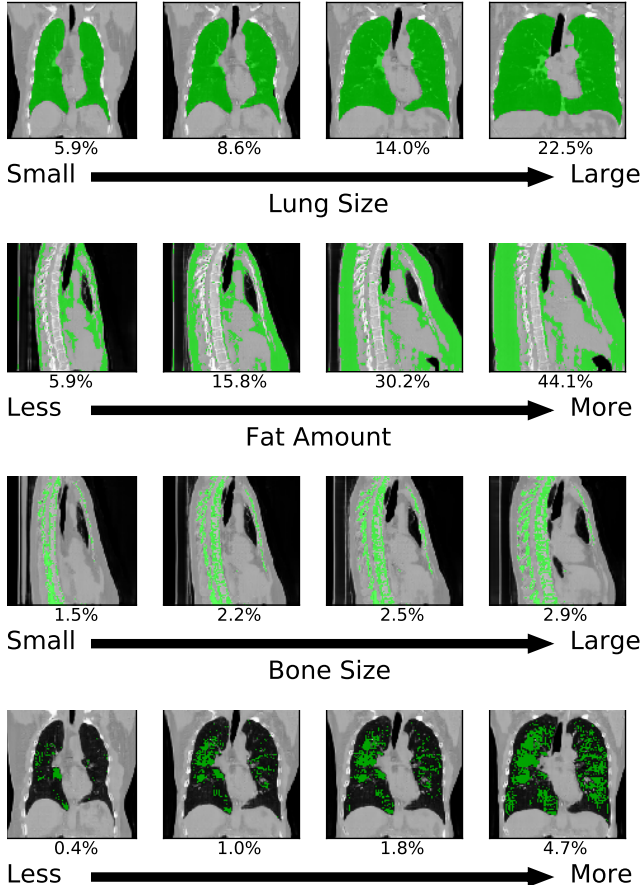


Fig. 7: Latent space exploration on thorax CT images. The figure reports synthetic images generated by changing the latent code in four different directions, corresponding to the lung, fat, bone volume as well as the proportion of emphysema. The number shown below each slice indicates the percentage of the volume of interest that occupies the synthetic image. The segmentation masks are plotted in green.

clinical-relevant feature extraction. In detail, the more information retained in the encoded variable, the better recovery of the original image. Table V and Fig. 4 illustrate that HA-GAN outperforms VAE-GAN and  $\alpha$ -GAN in terms of image recovery based on extracted latent variable. While the encoder and generator for VAE-GAN and  $\alpha$ -GAN can only process images of size  $128^3$ , the HA-GAN directly encodes and generates images of size  $256^3$ , thus it can recover images with higher quality.

In HA-GAN, the reconstruction loss in the objective function shown in Equations (6) and (7) are based on voxel-wise  $\ell_1$  losses, such that each voxel contributes equally to the loss function. However, as shown in some tasks for disease classifications [47], [48], some regions in the images are more important than others because they contain more clinical-relevant information. We want HA-GAN to focus on better reconstructing the details in these clinical-relevant regions. Therefore, we would like to introduce an attention mechanism to the model in future work.

Table VII shows that HA-GAN can better extract clinical-

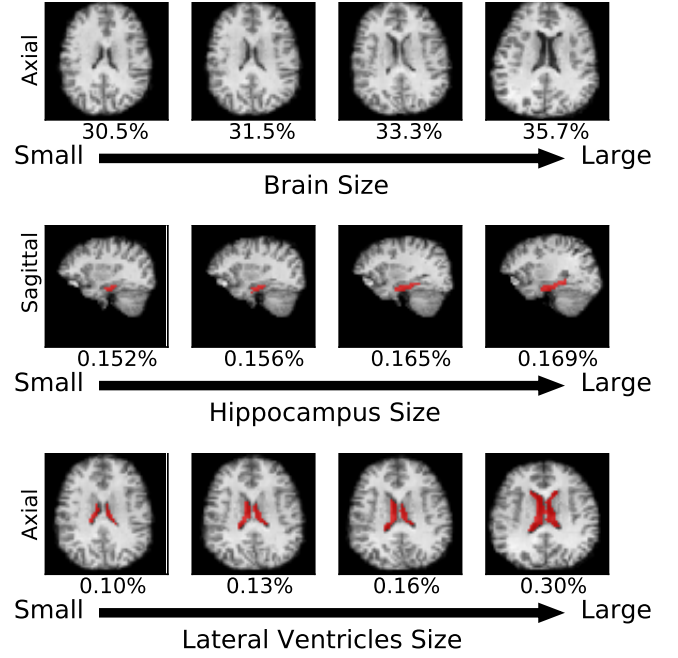


Fig. 8: Latent space exploration on brain MRIs. The figure reports synthetic images generated by changing the latent code in three different directions, corresponding to the brain's volumes, hippocampus, and lateral ventricles. The number shown below each slice indicates the percentage of the volume of interest that occupies the synthetic image. The segmentation masks are plotted in red.

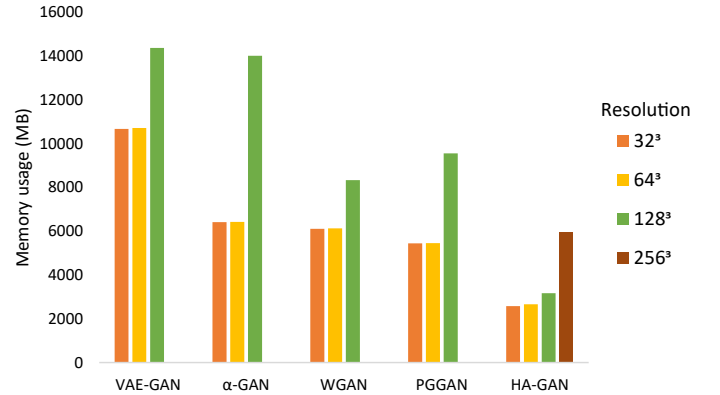


Fig. 9: Results of memory usage test. Note that only HA-GAN can generate images of size  $256^3$  without memory overflow.

relevant features from the images, comparing to VAE-GAN and  $\alpha$ -GAN. Some clinical-relevant information might be hidden in specific details in the medical images, and can only be observed under high-resolution. VAE-GAN and  $\alpha$ -GAN can only process lower-resolution images of  $128^3$ . We speculate that the high-resolution information leveraged by HA-GAN helps it learn representations that are more predictive for the clinical-relevant measurements.

Although our HA-GAN is capable of extracting clinical-relevant features, it is an unsupervised method. Research [49] shows that if we utilize some clinical-relevant supervisions during training, the model is better explaining the clinical-

relevant measurement. To achieve this, we plan to incorporate clinical-relevant measurements by maximizing the mutual information between the latent representation and the provided measurements in future work.

### C. Exploring Latent Space

Fig. 7 and Fig. 8 show that certain directions in the latent space learned by HA-GAN have semantic meanings. We can identify the directions in the latent space that correspond to each semantic meaning of interest. However, we realize that in the identified direction of latent space, some other factors of variations that are irrelevant to the semantic meaning of interest are also changing. For example, in Fig 7, the size of lung is increasing as the amount of emphysema increases; in Fig 8, as the brain size increases, the shape and orientation of the brain also change. This is because the latent representation learned is entangled [50], such that the change in the latent space corresponds to the change of multiple factors of variations. For example, the latent direction we learned for ventricle size may also contain a portion for brain size. It is challenging to learn a representation disentangled for ventricle size and brain size in an unsupervised way. In real data, these two variables are associated. To make sure the model learns disentangled representations, we need to introduce additional regularization terms in the objective function, making each latent variable independent with each other, as introduced in [51], [52].

### D. Memory Efficiency

Because of its hierarchical structure, HA-GAN process only one sub-volume of high-dimensional images rather than the entire image in each iteration during training. This makes HA-GAN more efficient than baselines in terms of memory usage in each iteration during training, as shown in Fig 9. In addition, We found that as the output resolution increases, the total number of model parameters doesn't increase much, this is expected because it only need few more convolutional layers. But as the multiplier factor increases, the memory usage increases drastically. Based on the experiment results, we believe that the memory efficiency mainly comes from the sub-volume scheme rather than model parameters. In addition, here we only use one level of sub-volume selection and down-sampling because it already drastically reduced the memory cost, we leave incorporating multiple levels of subvolumes and downsampling in our future work.

## VI. CONCLUSION

In this work, we develop an end-to-end hierarchical GAN model that can generate 3D high-resolution images. The model simultaneously generates a low-resolution version of an image and a randomly selected high-resolution sub-volume during training. In this way, the memory demand for generating high-resolution images is amortized. During inference, the model can directly generate full 3D high-resolution images. An encoder with a similar hierarchical structure is incorporated to extract features from images and prevent mode collapse. Experiments on 3D thorax CT and brain MRI show that the

proposed model achieves state-of-the-art performance in image synthesis and clinical-relevant feature extraction. Since GAN may omit certain objects but generate realistic-looking models [53], HA-GAN can be further improved by introducing an attention mechanism and incorporating the clinical-relevant side information. Here we show use-case scenarios of generating medical images from scratch based on unconditional HA-GAN and cross-modality transform based on conditional HA-GAN. Our method enables various real-world medical imaging applications that rely on high-resolution image analysis and generation.

## REFERENCES

- [1] I. Goodfellow, J. Pouget-Abadie, M. Mirza, B. Xu, D. Warde-Farley, S. Ozair, A. Courville, and Y. Bengio, "Generative adversarial nets," in *Advances in neural information processing systems*, 2014, pp. 2672–2680.
- [2] A. Brock, J. Donahue, and K. Simonyan, "Large scale GAN training for high fidelity natural image synthesis," in *International Conference on Learning Representations*, 2019.
- [3] M. Rosca, B. Lakshminarayanan, D. Warde-Farley, and S. Mohamed, "Variational approaches for auto-encoding generative adversarial networks," *arXiv preprint arXiv:1706.04987*, 2017.
- [4] C. Han, K. Murao, and S. Satoh, "H2019, 'learning more with less: Gan-based medical image augmentation'," *arXiv*, 1904.
- [5] H.-C. Shin, N. A. Tenenholtz, J. K. Rogers, C. G. Schwarz, M. L. Senjem, J. L. Gunter, K. P. Andriole, and M. Michalski, "Medical image synthesis for data augmentation and anonymization using generative adversarial networks," in *International workshop on simulation and synthesis in medical imaging*. Springer, 2018, pp. 1–11.
- [6] G. Kwon, C. Han, and D.-s. Kim, "Generation of 3d brain mri using auto-encoding generative adversarial networks," in *International Conference on Medical Image Computing and Computer-Assisted Intervention*. Springer, 2019, pp. 118–126.
- [7] K. Armanious, C. Jiang, M. Fischer, T. Küstner, T. Hepp, K. Nikolaou, S. Gatidis, and B. Yang, "Medgan: Medical image translation using gans," *Computerized Medical Imaging and Graphics*, vol. 79, p. 101684, 2020.
- [8] Y. Lei, T. Wang, Y. Liu, K. Higgins, S. Tian, T. Liu, H. Mao, H. Shim, W. J. Curran, H.-K. Shu *et al.*, "Mri-based synthetic ct generation using deep convolutional neural network," in *Medical Imaging 2019: Image Processing*, vol. 10949. International Society for Optics and Photonics, 2019, p. 109492T.
- [9] H. Uzunova, J. Ehrhardt, F. Jacob, A. Frydrychowicz, and H. Handels, "Multi-scale gans for memory-efficient generation of high resolution medical images," in *International Conference on Medical Image Computing and Computer-Assisted Intervention*. Springer, 2019, pp. 112–120.
- [10] B. Yu, L. Zhou, L. Wang, J. Fripp, and P. Bourgeat, "3d cgan based cross-modality mr image synthesis for brain tumor segmentation," in *2018 IEEE 15th International Symposium on Biomedical Imaging (ISBI 2018)*. IEEE, 2018, pp. 626–630.
- [11] N. Burgos, M. J. Cardoso, F. Guerreiro, C. Veiga, M. Modat, J. McClelland, A.-C. Knopf, S. Punwani, D. Atkinson, S. R. Arridge *et al.*, "Robust ct synthesis for radiotherapy planning: application to the head and neck region," in *International Conference on Medical Image Computing and Computer-Assisted Intervention*. Springer, 2015, pp. 476–484.
- [12] J.-Y. Zhu, T. Park, P. Isola, and A. A. Efros, "Unpaired image-to-image translation using cycle-consistent adversarial networks," in *Proceedings of the IEEE international conference on computer vision*, 2017, pp. 2223–2232.
- [13] C. Baur, S. Albarqouni, and N. Navab, "Generating highly realistic images of skin lesions with gans," in *OR 2.0 Context-Aware Operating Theaters, Computer Assisted Robotic Endoscopy, Clinical Image-Based Procedures, and Skin Image Analysis*. Springer, 2018, pp. 260–267.
- [14] A. Kitchen and J. Seah, "Deep generative adversarial neural networks for realistic prostate lesion mri synthesis," *arXiv preprint arXiv:1708.00129*, 2017.
- [15] M. J. Chuquicuma, S. Hussein, J. Burt, and U. Bagci, "How to fool radiologists with generative adversarial networks? a visual turing test for lung cancer diagnosis," in *2018 IEEE 15th international symposium on biomedical imaging (ISBI 2018)*. IEEE, 2018, pp. 240–244.

- [16] M. Frid-Adar, E. Klang, M. Amitai, J. Goldberger, and H. Greenspan, "Synthetic data augmentation using gan for improved liver lesion classification," in *2018 IEEE 15th international symposium on biomedical imaging (ISBI 2018)*. IEEE, 2018, pp. 289–293.
- [17] K. Lei, M. Mardani, J. M. Pauly, and S. S. Vasanawala, "Wasserstein gans for mr imaging: from paired to unpaired training," *IEEE Transactions on Medical Imaging*, 2020.
- [18] B. Murugesan, S. V. Raghavan, K. Sarveswaran, K. Ram, and M. Sivaprakasam, "Recon-glgan: A global-local context based generative adversarial network for mri reconstruction," in *International Workshop on Machine Learning for Medical Image Reconstruction*. Springer, 2019, pp. 3–15.
- [19] H. Zhao, H. Li, and L. Cheng, "Synthesizing filamentary structured images with gans," *arXiv preprint arXiv:1706.02185*, 2017.
- [20] J. M. Wolterink, A. M. Dinkla, M. H. Savenije, P. R. Seevinck, C. A. van den Berg, and I. Išgum, "Deep mr to ct synthesis using unpaired data," in *International workshop on simulation and synthesis in medical imaging*. Springer, 2017, pp. 14–23.
- [21] Z. Li, Y. Wang, and J. Yu, "Brain tumor segmentation using an adversarial network," in *International MICCAI Brainlesion Workshop*. Springer, 2017, pp. 123–132.
- [22] T. Joyce, A. Chatsias, and S. A. Tsaftaris, "Deep multi-class segmentation without ground-truth labels," 2018.
- [23] S. Singla, B. Pollack, J. Chen, and K. Batmanghelich, "Explanation by progressive exaggeration," in *Proceedings of the Eighth International Conference on Learning Representations (ICLR 2020)*, 2020.
- [24] H. Shan, Y. Zhang, Q. Yang, U. Kruger, M. K. Kalra, L. Sun, W. Cong, and G. Wang, "3-d convolutional encoder-decoder network for low-dose ct via transfer learning from a 2-d trained network," *IEEE transactions on medical imaging*, vol. 37, no. 6, pp. 1522–1534, 2018.
- [25] E. Simo-Serra, "Virtual thin slice: 3d conditional gan-based super-resolution for ct slice interval," in *Machine Learning for Medical Image Reconstruction: Second International Workshop, MLMIR 2019 Proceedings*, vol. 11905. Springer Nature, 2019, p. 91.
- [26] W. Jin, M. Fatehi, K. Abhishek, M. Mallya, B. Toyota, and G. Hamarneh, "Applying artificial intelligence to glioma imaging: Advances and challenges," *arXiv preprint arXiv:1911.12886*, 2019.
- [27] M. D. Cirillo, D. Abramian, and A. Eklund, "Vox2vox: 3d-gan for brain tumour segmentation," *arXiv preprint arXiv:2003.13653*, 2020.
- [28] P. K. Diederik, M. Welling *et al.*, "Auto-encoding variational bayes," in *Proceedings of the International Conference on Learning Representations (ICLR)*, vol. 1, 2014.
- [29] J. Donahue, P. Krähenbühl, and T. Darrell, "Adversarial feature learning," *arXiv preprint arXiv:1605.09782*, 2016.
- [30] X. Chen, Y. Duan, R. Houthoofd, J. Schulman, I. Sutskever, and P. Abbeel, "Infogan: Interpretable representation learning by information maximizing generative adversarial nets," in *Advances in neural information processing systems*, 2016, pp. 2172–2180.
- [31] J. Townsend, T. Bird, J. Kunze, and D. Barber, "Hilloc: lossless image compression with hierarchical latent variable models," in *International Conference on Learning Representations*, 2020.
- [32] A. B. L. Larsen, S. K. Sønderby, H. Larochelle, and O. Winther, "Autoencoding beyond pixels using a learned similarity metric," *arXiv preprint arXiv:1512.09300*, 2015.
- [33] I. Gulrajani, F. Ahmed, M. Arjovsky, V. Dumoulin, and A. C. Courville, "Improved training of wasserstein gans," in *Advances in neural information processing systems*, 2017, pp. 5767–5777.
- [34] T. Karras, T. Aila, S. Laine, and J. Lehtinen, "Progressive growing of GANs for improved quality, stability, and variation," in *International Conference on Learning Representations*, 2018.
- [35] E. A. Regan, J. E. Hokanson, J. R. Murphy, B. Make, D. A. Lynch, T. H. Beaty, D. Curran-Everett, E. K. Silverman, and J. D. Crapo, "Genetic epidemiology of copd (copdgene) study design," *COPD: Journal of Chronic Obstructive Pulmonary Disease*, vol. 7, no. 1, pp. 32–43, 2011.
- [36] A. J. Holmes, M. O. Hollinshead, T. M. O'keefe, V. I. Petrov, G. R. Fariello, L. L. Wald, B. Fischl, B. R. Rosen, R. W. Mair, J. L. Roffman *et al.*, "Brain genomics superstruct project initial data release with structural, functional, and behavioral measures," *Scientific data*, vol. 2, p. 150031, 2015.
- [37] B. Fischl, "Freesurfer," *Neuroimage*, vol. 62, no. 2, pp. 774–781, 2012.
- [38] M. Heusel, H. Ramsauer, T. Unterthiner, B. Nessler, and S. Hochreiter, "Gans trained by a two time-scale update rule converge to a local nash equilibrium," in *Advances in neural information processing systems*, 2017, pp. 6626–6637.
- [39] A. Gretton, K. M. Borgwardt, M. J. Rasch, B. Schölkopf, and A. Smola, "A kernel two-sample test," *Journal of Machine Learning Research*, vol. 13, no. Mar, pp. 723–773, 2012.
- [40] S. Chen, K. Ma, and Y. Zheng, "Med3d: Transfer learning for 3d medical image analysis," *arXiv preprint arXiv:1904.00625*, 2019.
- [41] Z. Wang, A. C. Bovik, H. R. Sheikh, and E. P. Simoncelli, "Image quality assessment: from error visibility to structural similarity," *IEEE transactions on image processing*, vol. 13, no. 4, pp. 600–612, 2004.
- [42] R. San Jose Estepar, J. C. Ross, R. Harmouche, J. Onieva, A. A. Diaz, and G. R. Washko, "Chest imaging platform: an open-source library and workstation for quantitative chest imaging," in *C66. LUNG IMAGING II: NEW PROBES AND EMERGING TECHNOLOGIES*. American Thoracic Society, 2015, pp. A4975–A4975.
- [43] S. J. Lee, J. Liu, J. Yao, A. Kanarek, R. M. Summers, and P. J. Pickhardt, "Fully automated segmentation and quantification of visceral and subcutaneous fat at abdominal ct: application to a longitudinal adult screening cohort," *The British journal of radiology*, vol. 91, no. 1089, p. 20170968, 2018.
- [44] Z. Wang, S. Gu, J. K. Leader, S. Kundu, J. R. Tedrow, F. C. Sciruba, D. Gur, J. M. Siegfried, and J. Pu, "Optimal threshold in ct quantification of emphysema," *European radiology*, vol. 23, no. 4, pp. 975–984, 2013.
- [45] T. Salimans, I. Goodfellow, W. Zaremba, V. Cheung, A. Radford, and X. Chen, "Improved techniques for training gans," in *Advances in neural information processing systems*, 2016, pp. 2234–2242.
- [46] I. Durugkar, I. Gemp, and S. Mahadevan, "Generative multi-adversarial networks," *arXiv preprint arXiv:1611.01673*, 2016.
- [47] S. Korolev, A. Safiullin, M. Belyaev, and Y. Dodonova, "Residual and plain convolutional neural networks for 3d brain mri classification," in *2017 IEEE 14th International Symposium on Biomedical Imaging (ISBI 2017)*. IEEE, 2017, pp. 835–838.
- [48] C. Yang, A. Rangarajan, and S. Ranka, "Visual explanations from deep 3d convolutional neural networks for alzheimer's disease classification," in *AMIA Annual Symposium Proceedings*, vol. 2018. American Medical Informatics Association, 2018, p. 1571.
- [49] S. Singla, M. Gong, S. Ravanbakhsh, F. Sciruba, B. Poczos, and K. N. Batmanghelich, "Subject2vec: generative-discriminative approach from a set of image patches to a vector," in *International Conference on Medical Image Computing and Computer-Assisted Intervention*. Springer, 2018, pp. 502–510.
- [50] Y. Bengio, A. Courville, and P. Vincent, "Representation learning: A review and new perspectives," *IEEE transactions on pattern analysis and machine intelligence*, vol. 35, no. 8, pp. 1798–1828, 2013.
- [51] I. Higgins, L. Matthey, A. Pal, C. Burgess, X. Glorot, M. Botvinick, S. Mohamed, and A. Lerchner, "beta-vae: Learning basic visual concepts with a constrained variational framework," 2016.
- [52] R. T. Chen, X. Li, R. B. Grosse, and D. K. Duvenaud, "Isolating sources of disentanglement in variational autoencoders," in *Advances in Neural Information Processing Systems*, 2018, pp. 2610–2620.
- [53] D. Bau, J.-Y. Zhu, J. Wulff, W. Peebles, H. Strobelt, B. Zhou, and A. Torralba, "Seeing what a gan cannot generate," in *Proceedings of the IEEE International Conference on Computer Vision*, 2019, pp. 4502–4511.